July 16, 2007

GMSB SUSY Models with Non Pointing Photons Signatures in ATLAS at the LHC

Damien Prieur

Laboratoire d'Annecy-le-Vieux de Physique des Particules (LAPP)
9 Chemin de Bellevue, BP 110, 74941 Annecy-le-Vieux CEDEX, France

Rutherford Appleton Laboratory (RAL)
Chilton, Didcot, OX11 0QX, United Kingdom

Abstract

The reconstruction of non-pointing photons is a key feature for studying Gauge Mediated Supersymmetry Breaking (GMSB) models at the LHC. In this note the polar angular resolution of the ATLAS electromagnetic calorimeter for non-pointing photons is characterized from a detailed simulation of the detector. Resulting performance is used to reconstruct GMSB events with a fast simulation program, taking into account reconstruction effects. Finally, the sensitivity in extracting the sparticles masses and the lightest neutralino lifetime is estimated.

Contents

1 Characterization of the polar angular resolution of the ATLAS electromagnetic calorimeter

1.1 Introduction

The required performance of the ATLAS electromagnetic calorimeter, in terms of energy and also of angular resolution, has been set by the most demanding physics channels, one of them being the $H \rightarrow \gamma\gamma$ (Higgs boson decaying to two photons). The resolution on the reconstructed invariant di-photon mass is strongly dependant on the polar angular resolution of the electromagnetic calorimeter. The granularity of the cells of the electromagnetic calorimeter has been designed so that the angular resolution for particle coming from the interaction point is better than 60 mrad/$\sqrt{E(\text{GeV})}$ [1]. For particles coming from a displaced secondary vertex, such as the photons predicted by Gauge Mediated Supersymmetry Breaking (GMSB) models, this resolution is worsened. The aim of this section is to characterize the polar angular resolution that it is possible to reach with the electromagnetic calorimeter for non-pointing photons. It is performed on fully simulated single photons, reconstructed with a non-validated version of the ATLAS software.

1.2 Production of simulated photons

This study has been done using a detailed simulation of the ATLAS detector (DICE/ATLSIM version 3.2.1 [2]). Several sets of single photons were generated inside the detector and have been fully simulated. Each of these sets consist of 50000 photons generated with $p_T = 60$ GeV. This value is typical of the energy of the photons produced by the decay of neutralinos in GMSB models. Photons were randomly generated so that they were uniformly distributed in the pseudo-rapidity range covered by the barrel and the end-cap part of the electromagnetic calorimeter, i.e. with $|\eta| < 2.5$. The non-pointing photons sets were generated at several different positions along the beam axis, from $Z_{\text{vertex}} = 0$ cm to 150 cm. No spread was applied on the generated vertex position.

1.3 Characterization of the polar angular resolution

In this section the polar angular resolution of the electromagnetic calorimeter to non-pointing photons is determined.

1.3.1 Principle

The capacity of extracting the particle directions relies on the accurate measurement of the position along η of the electromagnetic shower, in each layer of the electromagnetic calorimeter. The principle of this method is shown on figure 1. This method requires to have a parametrization of the shower depth for each layer. This has been done from a detailed simulation of the detector. The distances, from the beam axis $R(\eta)$ for the barrel part, and from the interaction point $Z(\eta)$ for the end cap part, are determined by the average position of the energy deposited by electromagnetic showers in each layer. This depth is fitted by second order polynomial functions for the barrel part, as shown on figure 2, that are defined as following:

Front layer

$$\begin{aligned} R_1(\eta) &= 156.78 - 1.8975\ \eta - 1.7668\ \eta^2 \quad (\eta < 0.8) \\ R_1(\eta) &= 150.32 - 7.1716\ \eta - 4.1008\ \eta^2 \quad (\eta > 0.8) \end{aligned} \tag{1}$$

Middle layer

$$\begin{aligned} R_2(\eta) &= 169.71 - 1.5311\ \eta - 6.4153\ \eta^2 \quad (\eta < 0.8) \\ R_2(\eta) &= 173.91 - 7.5648\ \eta - 1.8501\ \eta^2 \quad (\eta > 0.8) \end{aligned} \tag{2}$$

For the end cap part, the shower depth is constant with $Z_1 = 376$ cm and $Z_2 = 388$ cm respectively for the front and middle layers.

These parameterizations of the shower depth are the one used in the reconstruction algorithms from the ATHENA development release 7.2.0. They were updated in later reconstruction releases to account for geometry changes.

From these parameterizations of the shower depth, and from the two positions η_1 and η_2, the direction η_p of the particle, for the barrel and the end cap part, is reconstructed using the relations:

Barrel part

$$\sinh(\eta_p) = \frac{R_2(\eta_2)\sinh(\eta_2) - R_1(\eta_1)\sinh(\eta_1)}{R_2(\eta_2) - R_1(\eta_1)} \tag{3}$$

End cap part

$$\sinh(\eta_p) = (Z_2(\eta_2) - Z_1(\eta_1)) \left[\frac{Z_2(\eta_2)}{\sinh(\eta_2)} - \frac{Z_1(\eta_1)}{\sinh(\eta_1)} \right]^{-1} \tag{4}$$

The transformation from the polar angle θ to the pseudo-rapidity η is done through the usual relation $\eta = -\ln|\tan(\theta/2)|$, which leads to the following useful relations:

$$\cosh(\eta) = \frac{1}{\sin\theta} \qquad \sinh(\eta) = \frac{1}{\tan\theta} \qquad \tanh(\eta) = \frac{1}{\cos\theta} \tag{5}$$

1.3.2 Reconstruction of non-pointing photons

The reconstruction of the simulated photons was done using the ATLAS standard reconstruction algorithms from the ATHENA development release 7.2.0 [3]. During the simulation and reconstruction stages neither electronic noise nor pile-up effects were added. These last two effects will certainly contribute to decrease the reconstruction performance. The contributions should be at the level of 10% [1], however this point is not considered here and will have to be carefully studied from detailed simulations.

The standard reconstruction algorithms are tuned for pointing particles, hence their performance is not optimal when reconstructing non-pointing particles. When applied to non-pointing photons, the polar angular resolution from the standard reconstruction increases from 60 mrad/$\sqrt{E}$ [1] to 700 mrad/$\sqrt{E}$, for a z-position Z_{vertex} of the generation vertex varying from 0 to 100 cm, as shown on figure 9. This degradation has several origins:

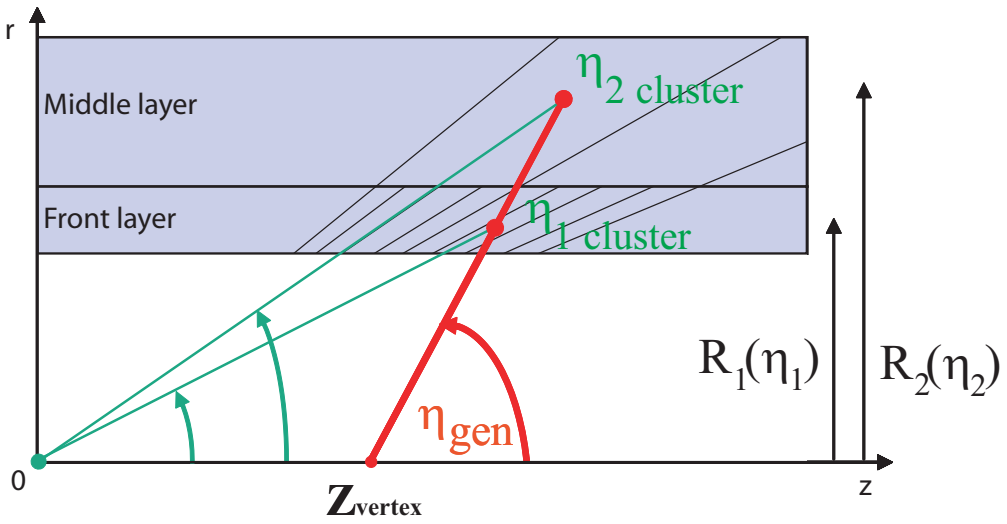

Figure 1: Sketch of the barrel part of the electromagnetic calorimeter and its first two layers showing the principle of the direction reconstruction for a photon generated at a distance Z_{vertex} from the ATLAS interaction point.

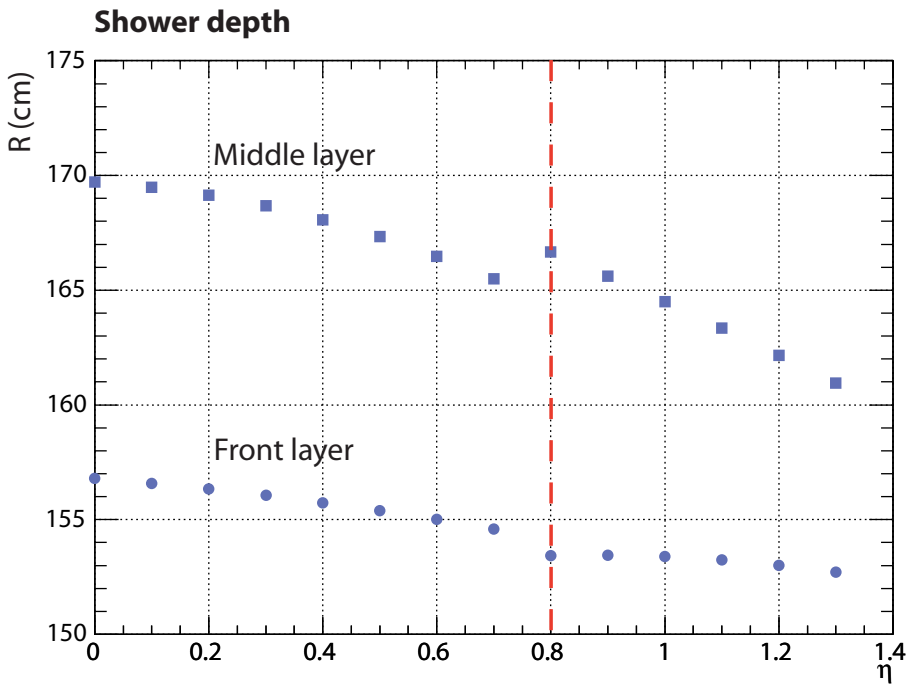

Figure 2: Parametrization of the electromagnetic shower depth extracted from a detailed simulation of the ATLAS detector, for the front and middle layers of the barrel part of the electromagnetic calorimeter. The red dashed line represents the change of sampling fraction at $\eta = 0.8$.

- The reconstruction of the position in each layer suffers of a systematic bias due to the finite size of the calorimeter cells, called the S-shape effect. In the standard reconstruction algorithms, the correction of this bias is tuned from pointing particles. For non-pointing photons this correction is no longer valid and contributes to the degradation of the angular resolution. In the following, an alternative method to correct for the S-shape bias is used. This method, called logarithmic weighting, takes into account the exponential fall off of the transversal shape of the shower to reconstruct its η position as following:

$$\overline{\eta} \equiv \frac{\sum \eta_i \omega_i}{\sum \omega_i} \quad \text{with} \quad \omega_i = \max\left[0, \omega_0 + \ln(E_i/E_c)\right] \tag{6}$$

  where the position η_i of the cell i is weighted by the ω_i coefficient. E_c is the total energy of the cluster and w_0 is a dimensionless free parameter. Studies performed on test beam data showed that in order to optimize the resolution the value of this parameter must be 2.0 and 4.4 respectively for the front and middle layers [4]. This method is used here to get rid of the S-shape bias for the middle layer. Concerning the front layer, since the size of the readout cells is smaller ($\Delta\eta_{\text{middle}} = 8\Delta\eta_{\text{front}}$), the S-shape bias is 10 times smaller and negligible, therefore no correction for the front layer cells is applied here.

- Another source of degradation comes from the finite size of the clusters. The electromagnetic shower of a non-pointing photon has a wider, non symmetrical, spatial extension. The standard cluster size is not wide enough to contain transversally such a shower, leading to energy leakage outside of the cluster (figures 3 and 4). To reduce these leakages, the size of the clusters is extended in this study to $\Delta\eta \times \Delta\phi = 5 \times 3$, in cell unit of the middle layer.

- Finally the parametrization of the shower depth, tuned for pointing photons, is no longer valid for such large incidence angles.

To estimate the bias introduced at the level of the reconstructed position, the true position η_{cluster} of the electromagnetic shower in the calorimeter must be computed out of the position Z_{vertex} of the generation vertex and the photon direction η_{gen}. This is done by solving for each layer these two equations:

Barrel part

$$\begin{aligned} \sinh(\eta_{1\text{ cluster}}) - \sinh(\eta_{\text{gen}}) &= \frac{Z_{\text{vertex}}}{R_1(\eta_{1\text{ cluster}})} \\ \sinh(\eta_{2\text{ cluster}}) - \sinh(\eta_{\text{gen}}) &= \frac{Z_{\text{vertex}}}{R_2(\eta_{2\text{ cluster}})} \end{aligned} \tag{7}$$

End cap part

$$\begin{aligned} \sinh(\eta_{1\text{ cluster}}) - \frac{L_1(\eta_{1\text{ cluster}})}{L_1(\eta_{1\text{ cluster}}) - Z_{\text{vertex}}}\ \sinh(\eta_{\text{gen}}) = 0 \\ \sinh(\eta_{2\text{ cluster}}) - \frac{L_2(\eta_{2\text{ cluster}})}{L_2(\eta_{2\text{ cluster}}) - Z_{\text{vertex}}}\ \sinh(\eta_{\text{gen}}) = 0 \end{aligned} \tag{8}$$

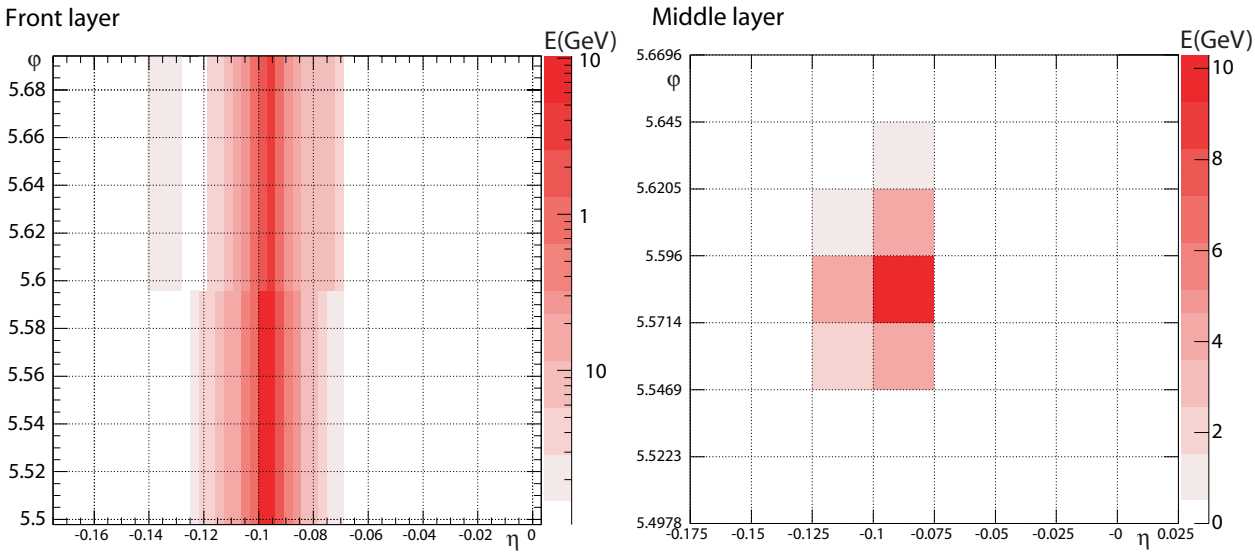

Figure 3: Event display of the energy deposited in the front and middle layers of the electromagnetic calorimeter for a pointing photon with $p_T = 60$ GeV.

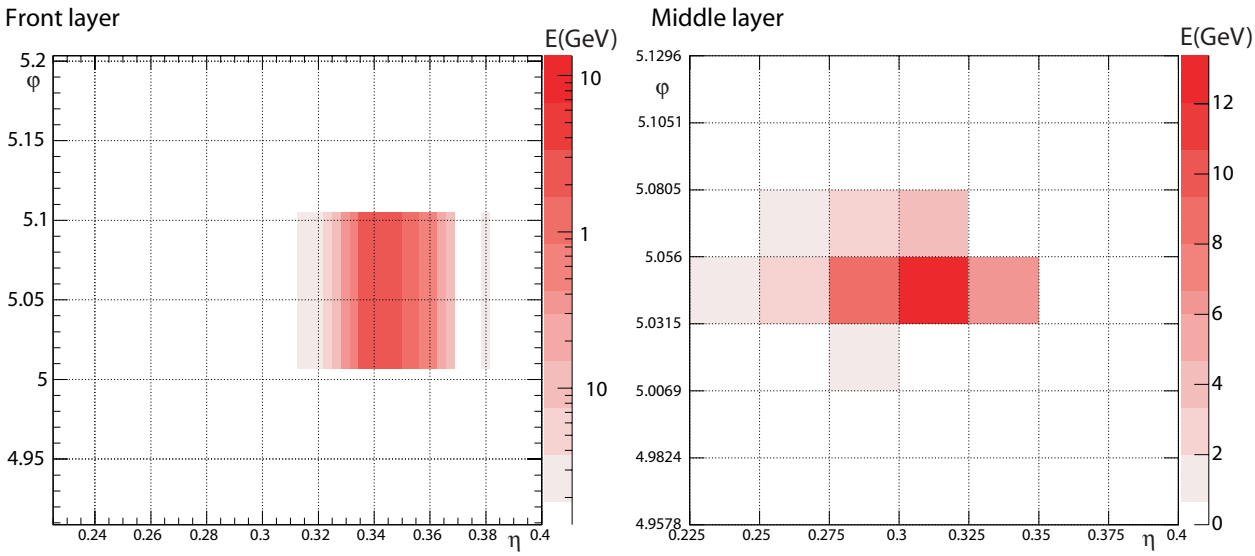

Figure 4: Event display of the energy deposited in the front and middle layers of the electromagnetic calorimeter for a non-pointing photon with $p_T = 60$ GeV, generated at $Z_{\text{vertex}} = 100$ cm. One can notice the difference of the average η position of the electromagnetic shower in the two layers due to the asymmetric shape of the non-pointing photon.

where R_i and L_i are the shower depth parameterizations, respectively for the barrel and the end cap parts.

The figure 5 shows the difference between the predicted position η_{pred} and the reconstructed one η_{rec} for middle layer cells. A systematic bias in the reconstructed position is clearly visible and this one increases with the value of Z_{vertex}. The same phenomenon can be seen for front layer cells but with a amplitude ten times smaller. This biased measurement of the position in the middle layer is the main restricting factor on the polar angular resolution for non-pointing particles.

For each Z_{vertex} value, fourth and second order polynomial functions, respectively for the barrel and for the end cap parts, are fitted to this bias. The variation of the coefficients defining these correction functions are interpolated by a second order polynomial functions. This allows to get a position correction function for each intermediate Z_{vertex} positions.

An iterative algorithm using the parametrization is used to correct for the position bias. From the position of the electromagnetic shower, the position of the generation vertex Z_{rec} is computed. Position corrections are then applied to each layer which allow to calculate a new position Z_{rec}. The algorithm loops until Z_{rec} converges, which usually takes two or three iterations.

Results of this correction on the reconstructed positions are shown on figures 6, 7 and 8 for the middle layer. For $|Z_{\text{vertex}}| < 100$ cm, the spread of these distributions decreases clearly. For $|Z_{\text{vertex}}| > 100$ cm, the algorithm efficiency is lower and improvements are less effective.

The angular resolution obtained after correction is shown on figures 9 and 10. For the barrel part and for small shifts of the vertex position ($Z_{\text{vertex}} < 10$ cm), the results are close to the 60 mrad/$\sqrt{E}$ expected from the standard reconstruction. For greater shifts ($Z_{\text{vertex}} > 30$ cm), the specific reconstruction algorithm for non-pointing photons allows to improve the angular resolution by 30% to 40% up to $Z_{\text{vertex}} = 100$ cm. Beyond, the improvement are less significative and would need a closer study of phenomena not taken into account here, such as the modification of the shower depth parametrization.

For the end cap part, the obtained resolution with the correction algorithm is systematically better by 40%, in particular for $Z_{\text{vertex}} = 0$ cm. This point shows that the used version of the reconstruction program was not properly optimized for this part of the calorimeter. This come from the previously mentioned bias in the position reconstruction for the middle layer. In that case, the non-pointing photon reconstruction algorithm minimizes these systematics biases and improves the angular resolution.

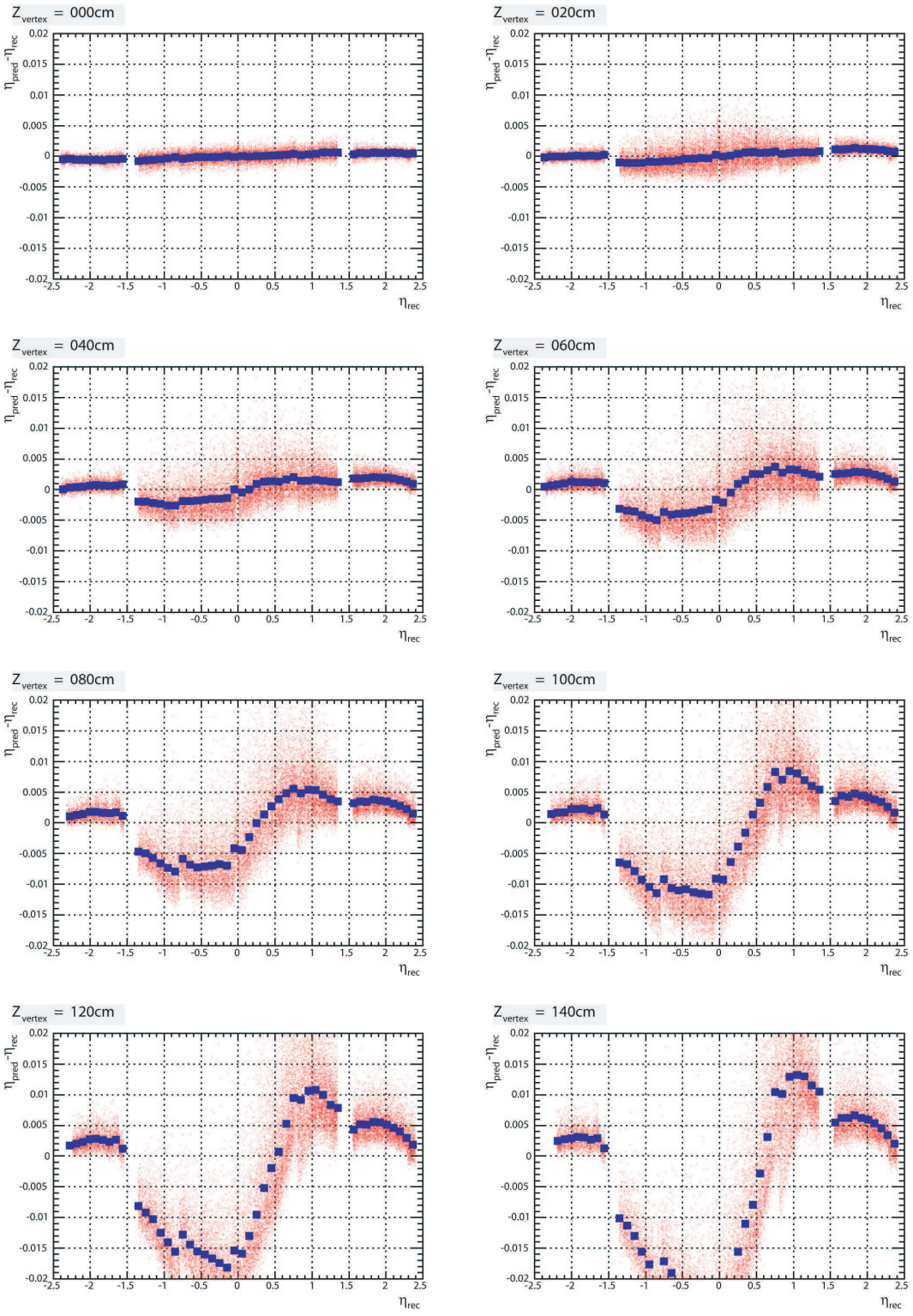

Figure 5: Scatter plot of the difference between the predicted position η_{pred} and the reconstructed one η_{rec} as a function of the position η_{rec} for middle layer cells of the calorimeter and for each value of Z_{vertex}. The blue squares represent the average distribution.

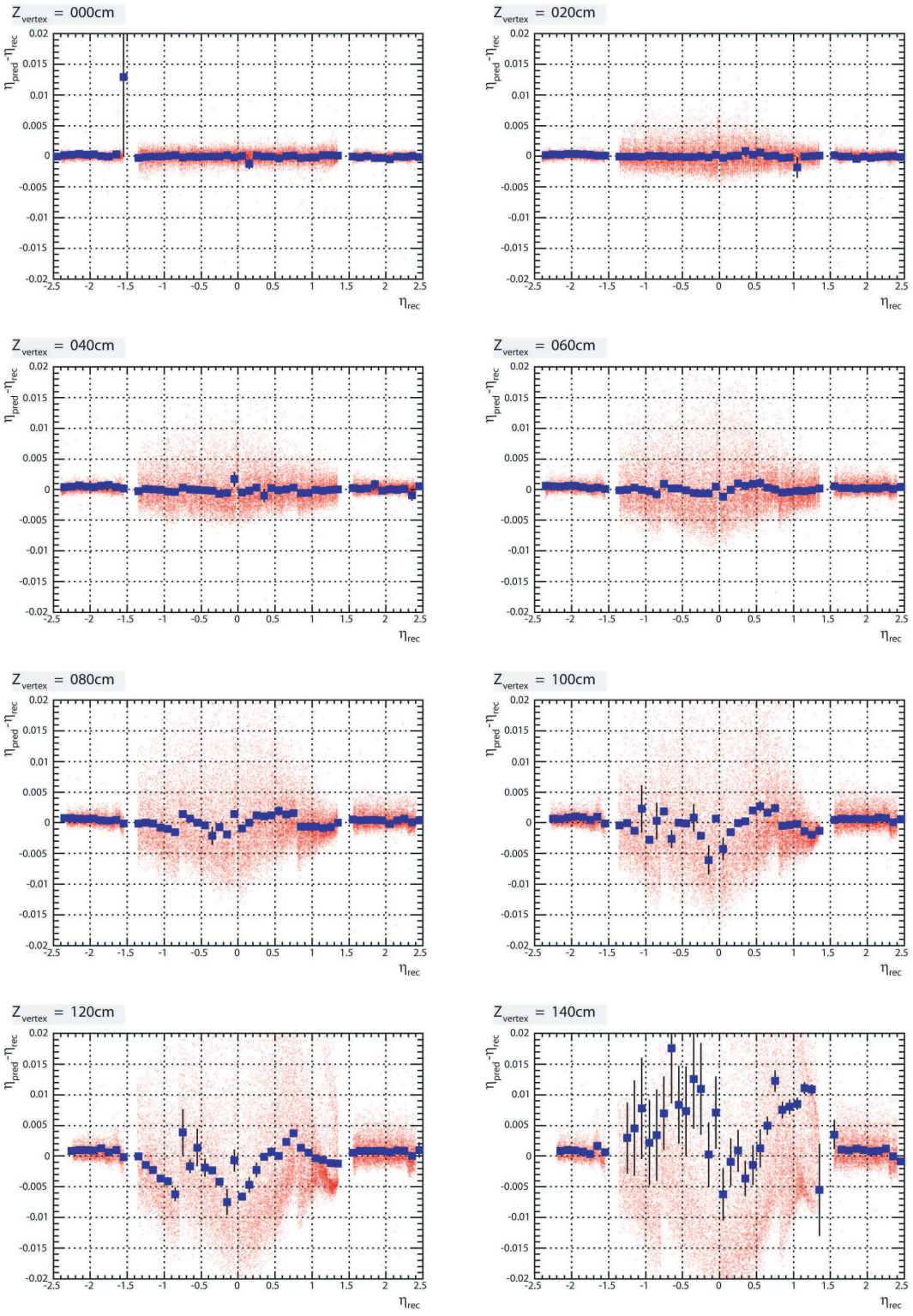

Figure 6: Scatter plot of the difference, after correction, between the predicted position η_{pred} and the reconstructed one η_{rec} is drawn as a function of the position η_{rec} for the middle layer cells and for each value of Z_{vertex}. The blue squares represent the average distribution.

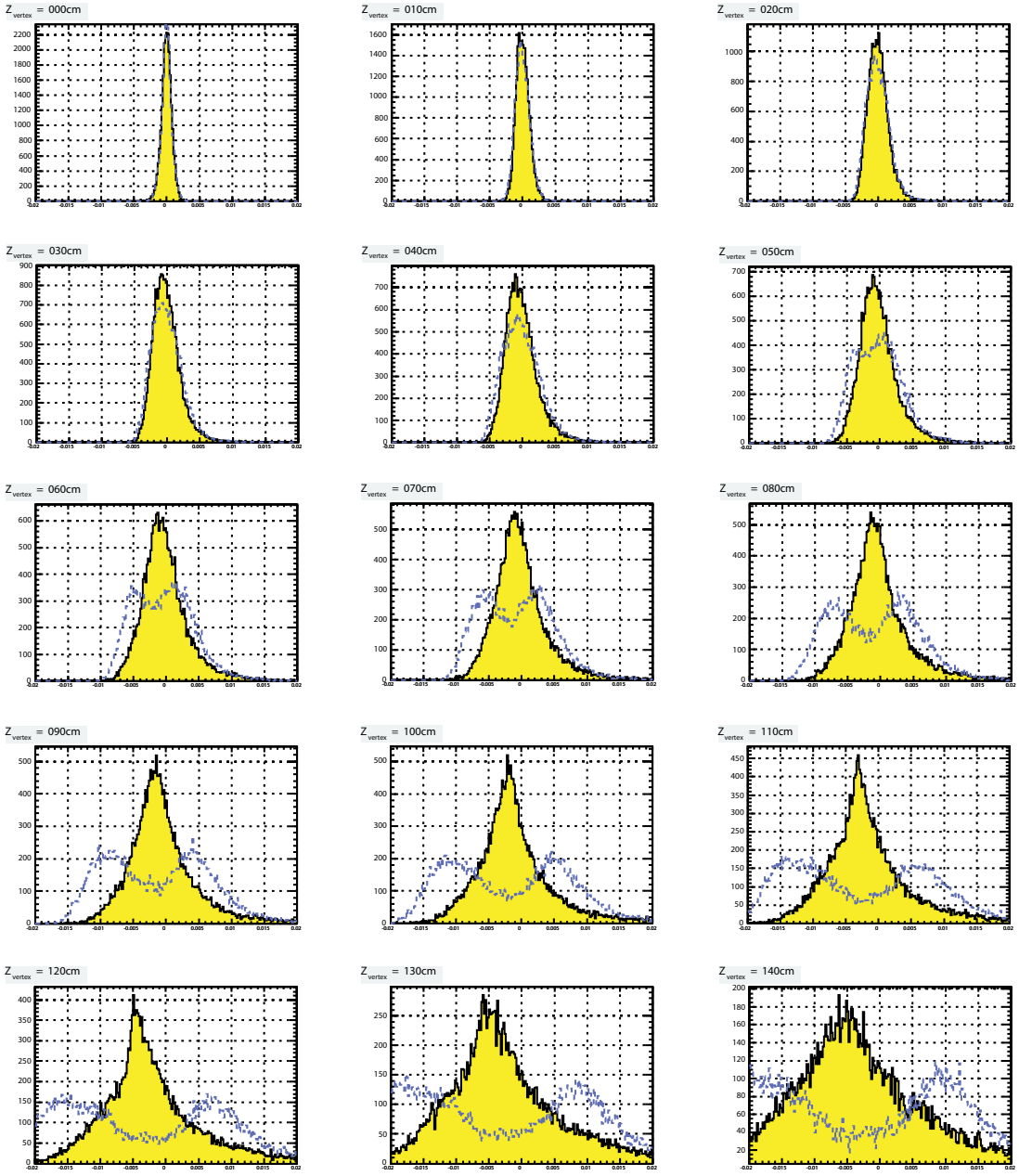

Figure 7: Distribution for each Z_{vertex} value of the difference between the predicted and the reconstructed position, before (dashed blue line) and after (yellow-filled distribution) corrections for the middle layer of the barrel part of the electromagnetic calorimeter.

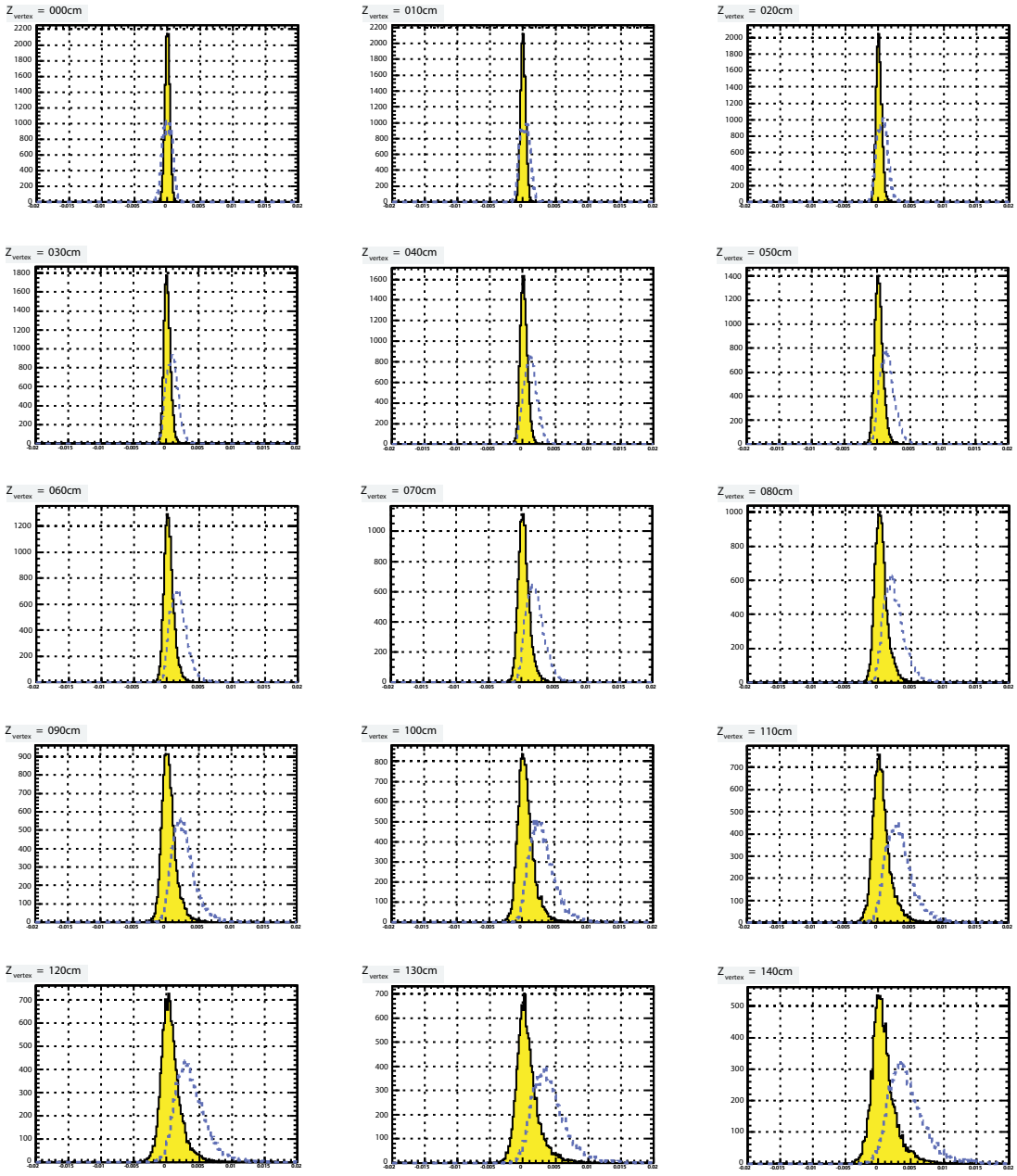

Figure 8: Distribution for each Z_{vertex} value of the difference between the predicted and the reconstructed position, before (dashed blue line) and after (yellow-filled distribution) corrections for the middle layer of the end cap part of the electromagnetic calorimeter.

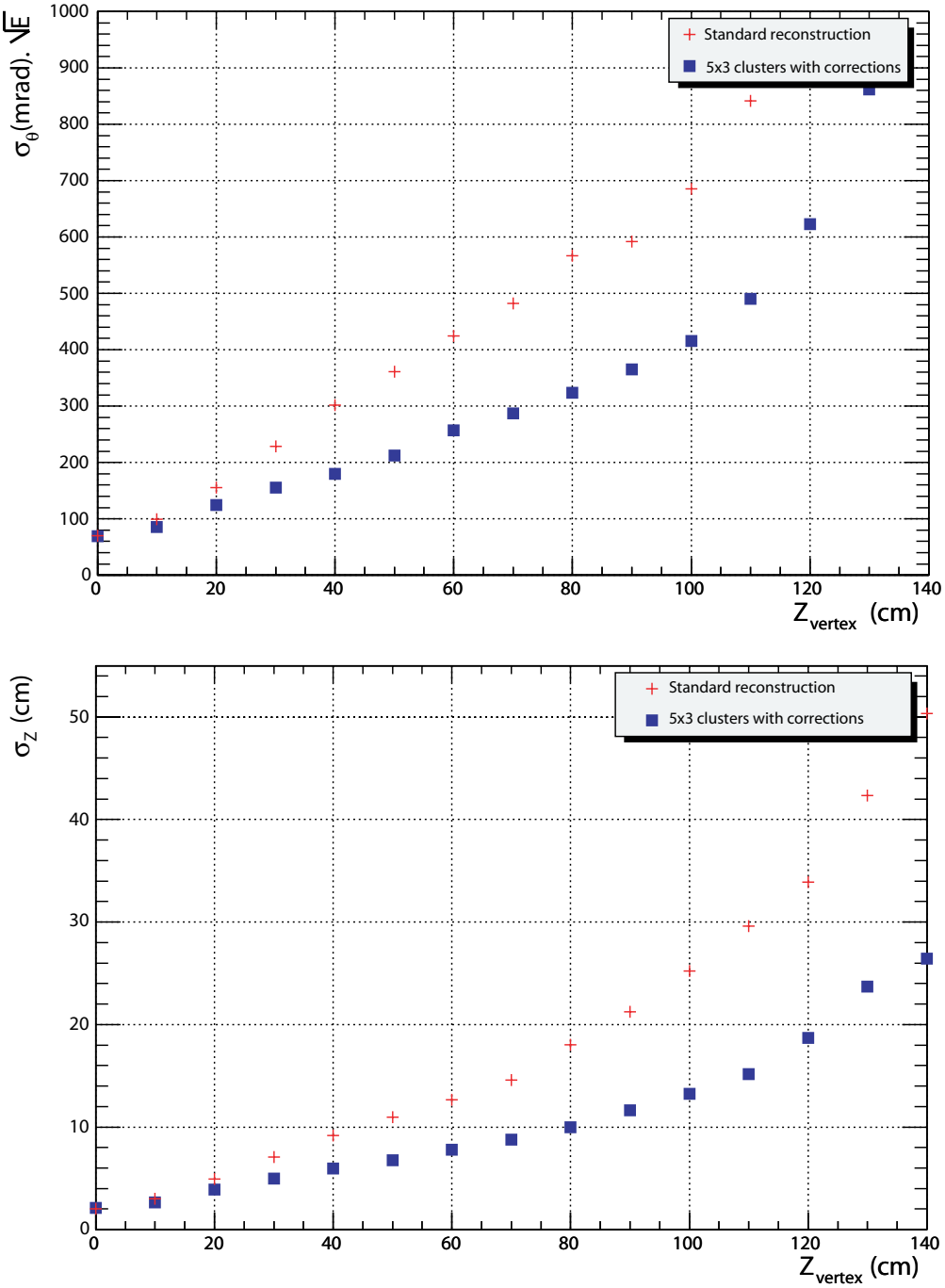

Figure 9: Angular resolution σ_θ and position resolution σ_Z on the generation vertex, before (red crosses) and after corrections (blue squares), for the barrel part of the electromagnetic calorimeter.

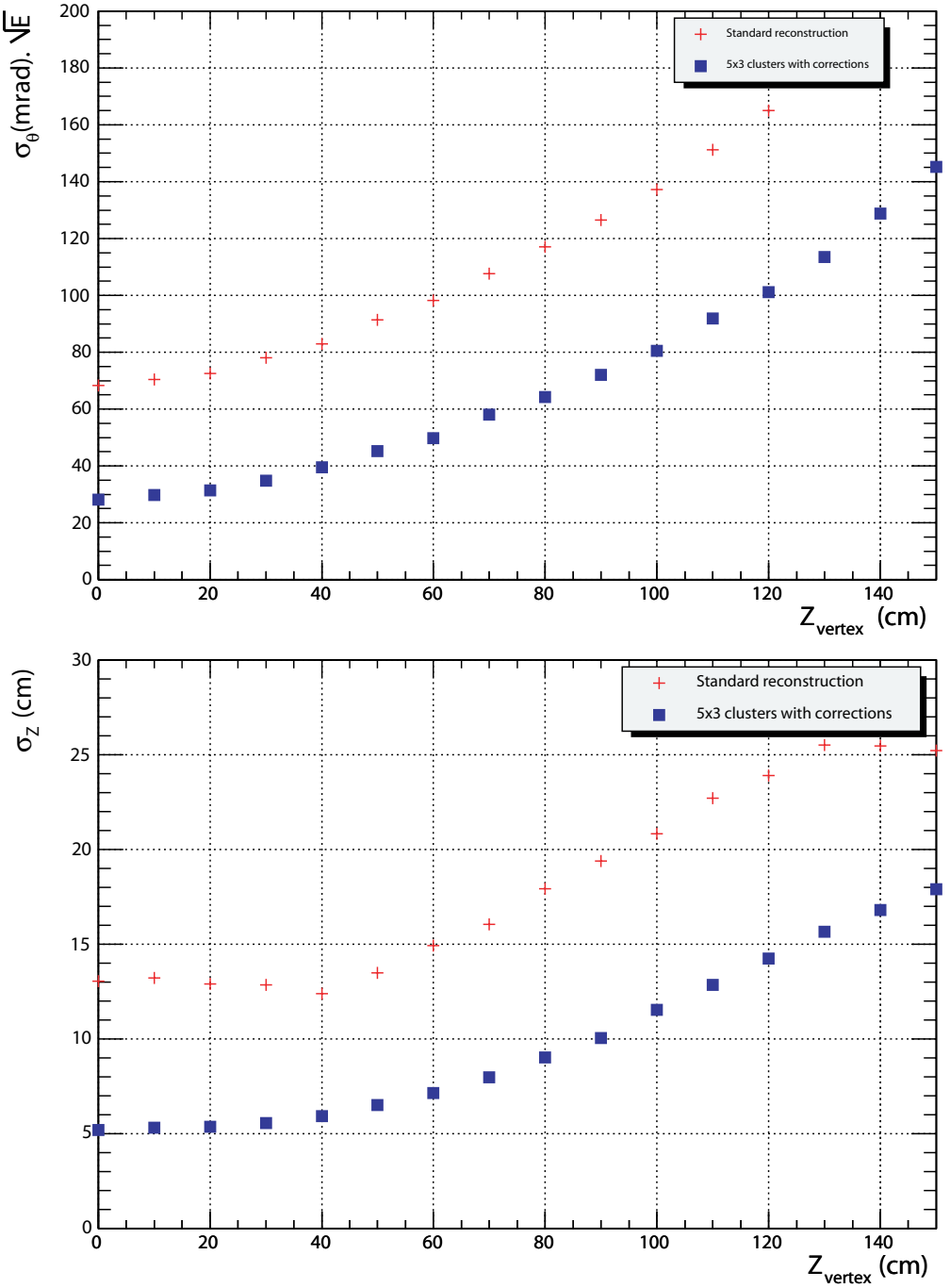

Figure 10: Angular resolution σ_θ and position resolution σ_Z on the generation vertex, before (red crosses) and after corrections (blue squares), for the end cap part of the electromagnetic calorimeter.

1.4 Conclusion

In this study, the ATLAS standard reconstruction algorithms, from the ATHENA development release 7.2.0, were used to reconstruct non-pointing photons. It comes out that a special treatment can be applied to improve the polar angular resolution of the electromagnetic calorimeter with respect to non-pointing photons. However this method has only a good efficiency for photons generated from an effective vertex with a position along the beam axis smaller than $Z = 100$ cm. Beyond, a detailed study of the shower depth for non-pointing photons would be mandatory to improve the efficiency of this method. A study on the transversal profile of non-pointing electromagnetic showers may also allow to extract alternative weighting methods to compute η barycenters and to minimize the associated systematic biases introduced.

The polar angular resolution finally achieved is acceptable for the decay channel studied in the next section. The resolution for the barrel and the end cap part of the electromagnetic calorimeter are parameterized using polynomial functions and integrated into a fast simulation of the ATLAS detector. The resulting performance in reconstructing the neutralino mass and lifetime is detailed in the next part.

2 Gauge Mediated Supersymmetry Breaking models and non-pointing photons

2.1 Introduction

The origin of the supersymmetry (SUSY) breaking and its mediation to the MSSM sector are key features of SUSY models. In Gauge Mediated SUSY Breaking (GMSB) models [5], the breaking of SUSY takes place in a hidden sector at a high energy scale $\sqrt{F_0}$. Contrary to SUGRA type models, SUSY breaking is not generated at the Planck scale but at a much lower energy scale. This breaking is then transmitted to the MSSM sector through chiral superfields belonging to an intermediate messenger sector at an energy scale M_{mess}. The coupling between the messenger and the MSSM sector is made through classical $SU(3)_c \otimes SU(2)_L \otimes U(1)_Y$ gauge interactions. Gravitational interactions are still present but their contributions are small. Since the gravitino $\widetilde{G}$ gets its mass only through gravitational interaction, it is the lightest SUSY particle (LSP). It is assumed here that the R-parity is a conserved quantity so that all heavier SUSY particles will decay into chains leading in the end to the production of gravitinos. The minimal GMSB model is driven by six arbitrary parameters. Depending on these parameters, the next to lightest SUSY particle (NLSP) can either be the lightest neutralino ($\widetilde{\chi}_1^0$) or a right handed slepton ($\widetilde{\ell}_R$). One of the feature of GMSB models is that the NLSP lifetime $c\tau$ may be macroscopic and can vary from micrometers up to kilometers. The value of $c\tau$ is linked to m_{NLSP} and to $\sqrt{F_0}$ through the relation [6]

$$c\tau = \frac{1}{k_\gamma}\left(\frac{100\text{ GeV}}{m_{\text{NLSP}}}\right)^5\left(\frac{\sqrt{F_0}}{100\text{ TeV}}\right)^4 \times 10^{-2}\text{ cm} \tag{9}$$

where $k_\gamma \equiv |N_{11}cos\theta_W + N_{12}sin\theta_W|$ with θ_W the Weinberg angle and N_{ij} the mixing angles of the neutralinos.

Measuring the NLSP lifetime provides a way to access $\sqrt{F_0}$, the fundamental supersymmetric breaking scale. This can be done by reconstructing the decay vertex of the neutralino from the photon direction and its arrival time.

This part is dedicated to the study of the following GMSB signal $\widetilde{\ell} \rightarrow \ell\widetilde{\chi}_1^0 \rightarrow \ell\gamma\widetilde{G}$, where the lightest neutralino $\widetilde{\chi}_1^0$ has a macroscopic lifetime generating a non-pointing photon in the final state. This analysis reproduces rigorously the one performed in [7], however it make use of a more detailed experimental treatment of the various sub-detectors. In particular the parameterized polar angular resolution of the electromagnetic calorimeter, determined in section 1, is used to characterize the performance of the reconstruction of sleptons and neutralinos masses and to determine the lightest neutralino lifetime.

2.2 Events kinematics

Neutralinos with an intermediate lifetime are considered so that the characteristic decay length is typically of the order of one meter. From the original method developed and described in [7], it becomes possible to reconstruct the gravitino direction and to access the sleptons $\widetilde{\ell}$ and neutralino $\widetilde{\chi}_1^0$ masses. Once these masses are known, one can determine the $\widetilde{\chi}_1^0$ decay vertex position and extract its lifetime.

Figure 11 represents the typical topology of a neutralino decay inside the ATLAS detector. It is produced at time $t = 0$ at the center of the detector and it decays at time t_D (M point)

into one photon and one gravitino. To reconstruct the position of the $\widetilde{\chi}_1^0$ decay vertex, it is essential to be able to determine the photon direction (α angle) and its arrival time t_γ in the electromagnetic calorimeter. From these observables, the ψ angle, between the photon and the gravitino, is determined from the following relations:

$$\begin{aligned} \cos\ \psi &= \frac{1-\xi^2}{1+\xi^2} \\ \text{with}\quad \xi &= \frac{ct_\gamma + L(1-\cos\alpha)}{L\sin\alpha} \end{aligned} \tag{10}$$

where L is the distance between the interaction point O and the impact point A in the electromagnetic calorimeter. From the ψ angle and the photon momentum $\overrightarrow{p_\gamma}$, the gravitino momentum $\overrightarrow{p_{\widetilde{G}}}$ can be fully determined.

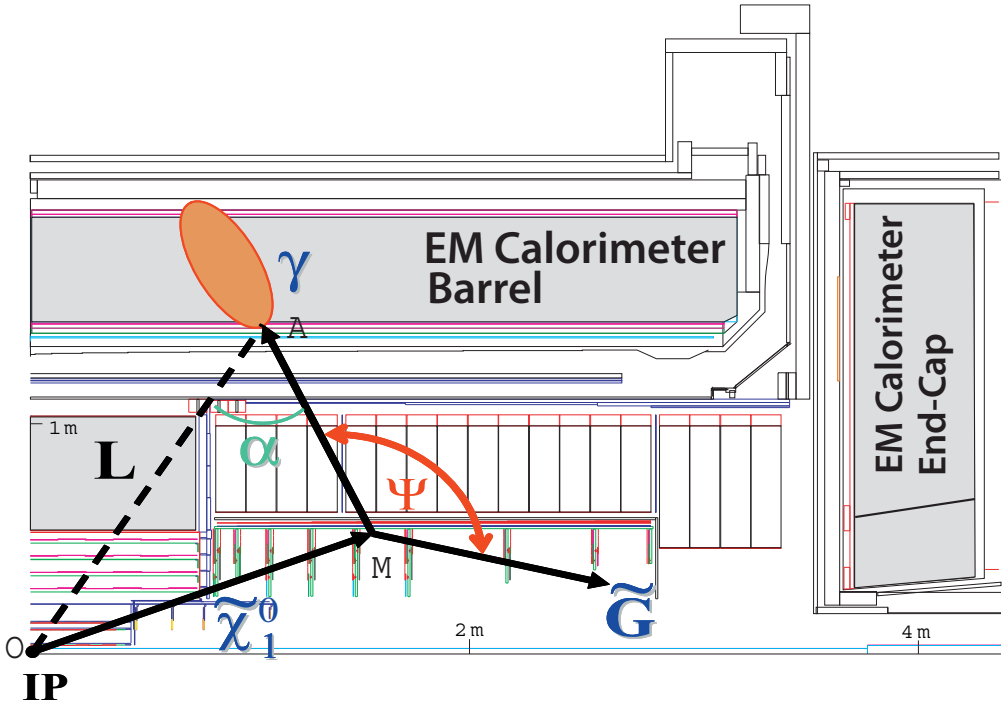

Figure 11: Graphical representation of a $\widetilde{\chi}_1^0$ decay into one gravitino and one photon inside the ATLAS detector.

As the slepton and the neutralino belong to the same decay chain, it is possible to establish a relation between the slepton mass $m_{\widetilde{\ell}}$ and the neutralino mass $m_{\widetilde{\chi}_1^0}$. This last mass can be expressed as

$$\begin{aligned} m^2_{\widetilde{\chi}_1^0} &= \left(p_\gamma + p_{\widetilde{G}}\right)^2 \\ &= 2E_\gamma E_{\widetilde{G}}\left(1-\cos\psi\right) \end{aligned} \tag{11}$$

The invariant mass $m^2_{\widetilde{\ell}}$ can be written as

$$m^2_{\widetilde{\ell}} = \left(p_\gamma + p_{\widetilde{G}} + p_\ell\right)^2 \tag{12}$$

Using relation 11 and neglecting gravitino and lepton masses leads to this expression

$$m_{\tilde{\ell}}^2 = \left(1 + \frac{E_\ell(1-\cos\theta_{\tilde{G}\ell})}{E_\gamma(1-\cos\psi)}\right) m_{\tilde{\chi}_1^0}^2 + 2E_\ell E_\gamma(1-\cos\theta_{\ell\gamma}) \quad (13)$$

$$\equiv am_{\tilde{\chi}_1^0}^2 + b \quad (14)$$

where a and b parameters are defined accordingly

$$a \equiv \left(1 + \frac{E_\ell(1-cos\theta_{\tilde{G}\ell})}{E_\gamma(1-\cos\psi)}\right) \quad (15)$$

$$b \equiv 2E_\ell E_\gamma(1-\cos\theta_{\ell\gamma}) \quad (16)$$

The E_ℓ, E_γ, $\cos\psi$, $\cos\theta_{\tilde{G}\ell}$ and $\cos\theta_{\ell\gamma}$ quantities being all measured, the a and b parameters can be computed for each event. If points of coordinates (a,b) are placed in a plane, they will regroup along the line of equation $b = m_{\tilde{\ell}}^2 - am_{\tilde{\chi}_1^0}^2$. Each event from the considered decay chain adds an independent constraint to determine $m_{\tilde{\ell}}$ and $m_{\tilde{\chi}_1^0}$ masses.

2.3 Event generation and simulation

In this study the standard set of GMSB parameters called $G1$ [8] (table 1) is chosen. At this point, sleptons and neutralino masses are respectively of 161.4 and 117.1 GeV (table 2). 10^5 events were generated with HERWIG [9], corresponding to one year of LHC running at low luminosity (10 fb^{-1}). These events were passed through ATLFAST [10], the fast simulation of the ATLAS detector, which smears particles observables according to each sub-detector performance. At this level, the NLSP is kept stable and is decayed only at the analysis stage, depending on the input characteristics decay time $c\tau$.

Further in the analysis, a conversion into an e^+e^- pair of the photon coming from the neutralino is required. This conversion is done at the analysis stage and the conversion rate is tuned so that 30% of the photons are converted in the volume of the inner detector. This conversion rate is extracted from the datasets described in section 1.2

Point	Λ (TeV)	M_{mess} (TeV)	N_5	$\tan\beta$	sgn(μ)	C_{grav}
G1	90	500	1	5.0	+	-

Table 1: GMSB model parameters at point $G1$ [8]. C_{grav} is a free parameter linked to the gravitino mass and to the NLSP decay length. Topology of GMSB events depends on the C_{grav} value.

The resolutions used to smear non-pointing photons observables are summarized in table 3. The energy resolution is parameterized according to the electromagnetic calorimeter performance measured during test beam. The noise term, 245 MeV/$\sqrt{E}$, corresponds to the expected noise for fixed size clusters ($\Delta\eta \times \Delta\phi = 0.125 \times 0.075$) at low luminosity. The resolution on photon arrival time is 100 ps, however this value remain conservative since test beams have shown that a better time resolution could be achieved [12]. The measurement of the electromagnetic shower position is done accordingly to these resolutions, $\sigma_\eta = 0.004/\sqrt{E(\text{GeV})}$ and $\sigma_\phi = 5$ mrad$/\sqrt{E(\text{GeV})}$. These two values are reasonable approximations of the real resolutions which vary with the η position of the electromagnetic shower.

Particle	Mass (GeV)	Particle	Mass (GeV)	Particle	Mass (GeV)
$\widetilde{g}$	733	$\widetilde{u}_L$	958	$\widetilde{e}_L$	324
$\widetilde{\chi}_1^\pm$	218	$\widetilde{u}_R$	915	$\widetilde{e}_R$	161
$\widetilde{\chi}_2^\pm$	456	$\widetilde{d}_L$	961	$\widetilde{\nu}_e$	315
$\widetilde{\chi}_1^0$	117	$\widetilde{d}_R$	911	$\widetilde{\tau}_1$	161
$\widetilde{\chi}_2^0$	218	$\widetilde{t}_1$	824	$\widetilde{\tau}_2$	324
$\widetilde{\chi}_3^0$	436	$\widetilde{t}_2$	938	$\widetilde{\nu}_\tau$	314
$\widetilde{\chi}_4^0$	457	$\widetilde{b}_1$	909	h	109
		$\widetilde{b}_2$	919	H	545
				A	543
				$H^\pm$	549

Table 2: Supersymmetic particle masses at GMSB point $G1$ (table 1) generate from ISAJET 7.64 [11]. The first two squarks generations being degenerated in mass, only the first one is shown. Gravitino mass is not indicated since it depends on C_{grav} which is not a fixed parameter in this study.

The resolution σ_θ on the measurement of the polar angle θ was determined in section 1. If the electromagnetic calorimeter can be used to obtain the polar angle of the incident photon, its bad granularity along the ϕ direction does not allow to determine the photon direction in the $R\phi$ plane. Since this information is mandatory for the first part of the analysis in order to compute the $\widetilde{\ell}$ and $\widetilde{\chi}_1^0$ masses, converted photons are required. About 20 to 30% of the photons are converted into an e^+e^- pair inside the volume of the inner detector. For such converted photons, the transition radiation tracker (TRT) can be used to get the ϕ direction with a $\sigma_{\Delta\phi} = 1$ mrad resolution [13]. However, the reconstruction efficiency for such tracks would need a careful study relied on a detailed simulation of the detector, this was not performed here.

Observable	Detector	Resolution
Energy	EM CAL.	$\frac{\delta E}{E} = \frac{10\%}{\sqrt{E}} \oplus \frac{245\ \text{MeV}}{E} \oplus 0.7\%$
Time	EM CAL.	$\sigma_t = 100$ ps
Position	EM CAL.	$\sigma_\eta = \frac{0.004}{\sqrt{E(\text{GeV})}}$, $\sigma_\phi = \frac{5\ \text{mrad}}{\sqrt{E(\text{GeV})}}$
Direction	EM CAL.	σ_θ
	TRT	$\sigma_{\Delta\phi} = 1$ mrad

Table 3: Resolutions used to smear the reconstructed observables of non-pointing photons during the analysis stage.

2.4 Reconstruction of sparticle masses

The method describe in 2.2 is used here to reconstruct the $m_{\widetilde{\ell}}$ and $m_{\widetilde{\chi}_1^0}$ masses. This requires the knowledge of the complete photon direction, along η and ϕ. That is why it is required here that the photons coming from the $\widetilde{\chi}_1^0$ converts into an e^+e^- pair inside the volume of the

inner detector where they can be efficiently reconstructed ($r < 80$ cm and $|z| < 280$ cm). The neutralino lifetime is arbitrary fixed to $c\tau = 100$ cm. Hence, a large part of the neutralinos will decay inside the TRT volume (radius $r = 107$ cm and half length $z = 300$ cm).

Standard pre-selection cuts are applied to suppress noise contributions from the standard model. The complete background analysis was not realized here, cuts from [14] were used instead to keep standard model noise contributions to a negligible level.

To be selected, an event must have at least 4 jets and satisfy the following conditions:

$$\begin{aligned} M_{\text{eff}} &> 400 \text{ GeV} \\ E_T^{\text{miss}} &> 0.1 M_{\text{eff}} \end{aligned} \tag{17}$$

where E_T^{miss} is the missing transverse energy and M_{eff} an effective mass defined by the sum of the missing E_T and the transverse momentum of the four hardest jets:

$$M_{\text{eff}} \equiv E_T^{\text{miss}} + p_{T,1} + p_{T,2} + p_{T,3} + p_{T,4} \tag{18}$$

This cut, represented on figure 12, keeps 93% of the generated events. Since sparticles are pair-produced (it is assumed here that the R-parity is a conserved quantity), each event is required to have at least two photons and two isolated leptons. This last cut has an efficiency of 21% and accepted events are the source of about 29000 $\widetilde{\chi}_1^0$.

About 53% of the produced neutralinos decay in the inner detector and only 24% of them are converted. The following cuts are then sequentially applied to select good non-pointing photons candidates:

$$\begin{aligned} E_\gamma &> 30 \text{ GeV} \\ \alpha &> 0.2 \text{ rad} \\ \Delta t_\gamma &> 1 \text{ ns} \end{aligned} \tag{19}$$

where $\Delta t_\gamma \equiv t_\gamma - L/c$ is the difference between the arrival time recorded by the electromagnetic calorimeter and the time that a direct pointing photon would have taken. These cuts are shown on figures 13, 14 and 15. Their efficiencies are respectively of 92, 23 and 75%. The E_γ cut rejects 85% of the pointing photons, but the cut on the α angle remains the most constraining and allows to reject all the pointing photons since pointing photons generated with $|Z_{\text{vertex}}| < 10$ cm have $\alpha < 0.05$. This very tight cut should be optimized; it has not done here in order to remain as close as possible to the study from [7]. We finally end up with 594 non-pointing photons. The resolution on the ψ angle, between the photon and the gravitino, is $\sigma_\psi = 60$ mrad as shown on figure 16.

To compute for each event the a and b parameters, and so to extract the $m_{\widetilde{\ell}}$ and $m_{\widetilde{\chi}_1^0}$ masses, non-pointing photons need to be paired with a lepton (either electron or muon). Leptons are required to have a minimum transverse energy of 20 GeV. The efficiency of this cut is 46%. If several leptons are available, only the one which minimizes the lepton-photon invariant mass $m_{\ell\gamma}$ is selected.

Figure 17 shows the distribution of the a and b parameters, computed for each lepton-photon pair, in the corresponding parameter space plane. Points group along the line of slope $-m_{\widetilde{\chi}_1^0}$ and intercept the y-axis at $m_{\widetilde{\ell}}$. Points which are deviating from the average

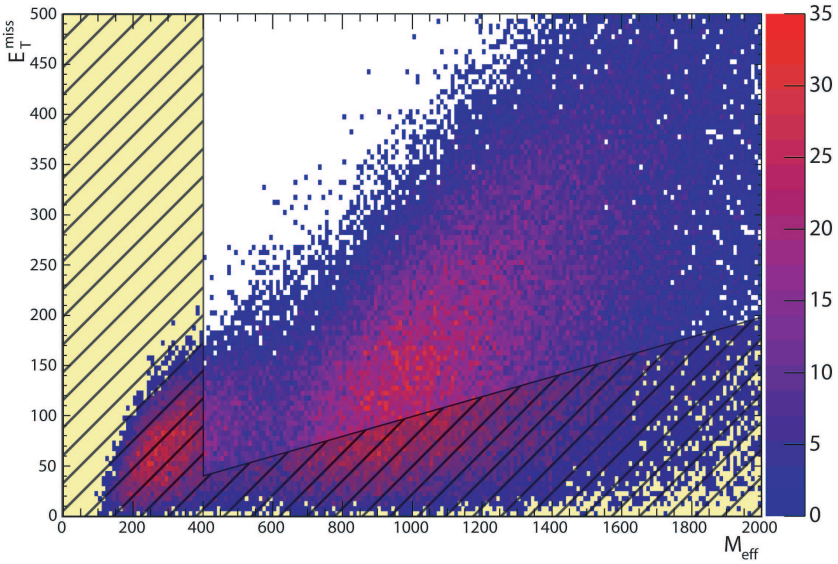

Figure 12: Effective mass M_{eff} and missing transverse energy E_T^{miss} distribution for events generated at GMSB point $G1$. The yellow-hatched area is rejected by the cuts from equation 17.

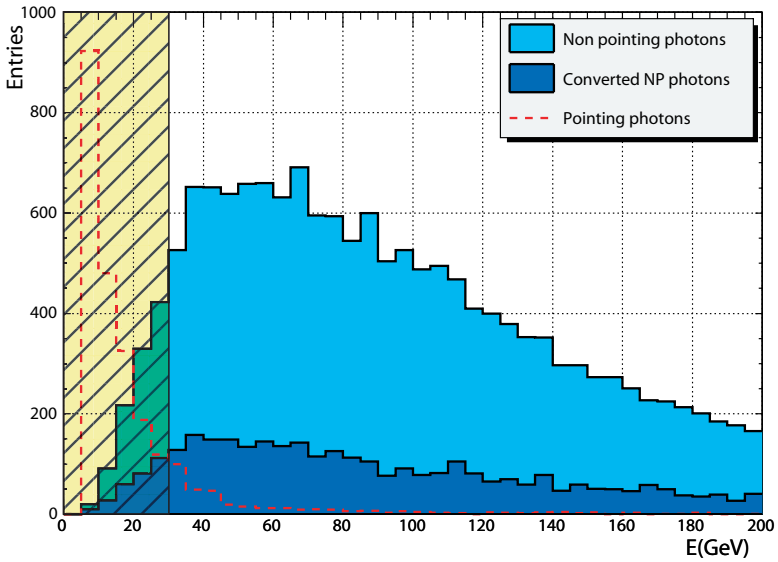

Figure 13: Energy distribution E_γ of the detected non-pointing photons (dark blue) and the ones converted inside the inner detector (light blue). The red distribution represents the energy spectrum of pointing photons. The yellow-hatched area is rejected by the cuts from equation 19.

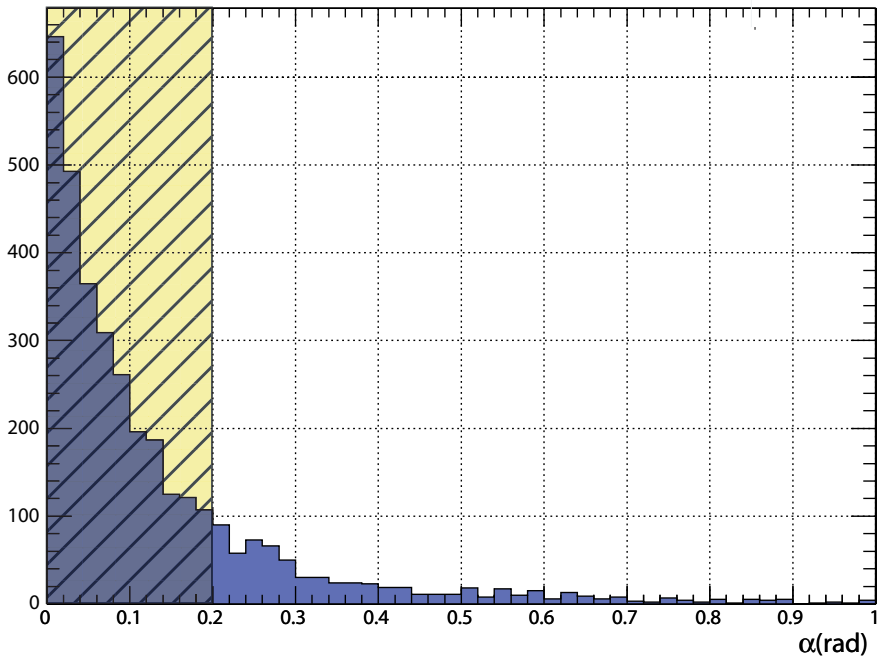

Figure 14: α angle distribution of the selected non-pointing photons. The yellow-hatched area is rejected by the cuts from equation 19.

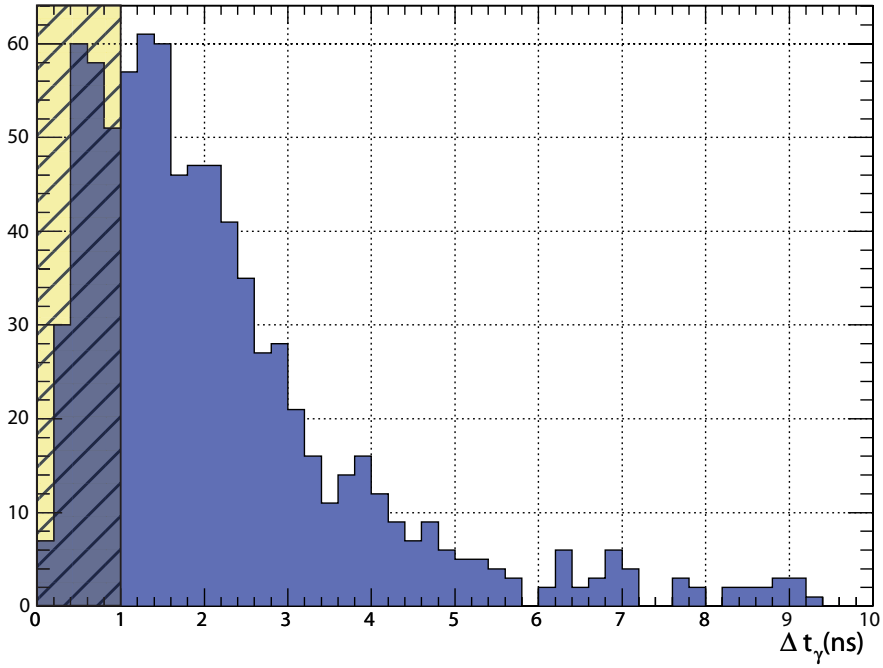

Figure 15: Δt_γ arrival time distribution of the selected non-pointing photons. The yellow filled area is rejected by the cuts from equation 19.

distribution come from bad lepton-photon pairing or from poorly reconstructed photon direction. A detailed analysis work is required here to work out discriminating topological or kinematical variables in order to reduce the pairing efficiency.

A selection area is arbitrary defined: the right plot on figure 17 represents the averaged distribution of the selected points. The fit of the distribution by a linear function gives the following results:

$$\begin{aligned} m_{\tilde{\chi}_1^0} &= 115.5 \text{ GeV} \\ m_{\tilde{\ell}} &= 159.9 \text{ GeV} \end{aligned} \tag{20}$$

that should be compared to the input values respectively of 117.1 and 161.4 GeV.

To estimate the error on the mass determination, the simulation is reproduced independently one hundred times . Results are shown on figure 18 where each distribution is fitted by a Gaussian. The standard deviations on masses measurement are $\sigma_{m_{\tilde{\chi}_1^0}} = 1.7$ GeV and $\sigma_{m_{\tilde{\ell}}} = 2.1$ GeV, corresponding to an 1.5% relative error.

As comparison, with a fixed angular resolution of 60 *mrad*, the sensitivity would have been smaller by 30 to 40% ($\sigma_{m_{\tilde{\chi}_1^0}} = 1.2$ GeV and $\sigma_{m_{\tilde{\ell}}} = 1.3$ GeV). The biases on reconstructed masses would also have been reduced, with $m_{\tilde{\chi}_1^0} = 116.2$ GeV and $m_{\tilde{\ell}} = 160.7$ GeV.

This deterioration of reconstruction performance with the decrease of the angular resolution is linked to the degradation of the ψ angle determination. The resolution on this angle is tabulated in table 4.

$\sigma_\theta(\text{mrad}) \times \sqrt{E}$	60	100	200	300	400	500	1000
$\sigma_\psi(\text{mrad})$	32	36	42	50	56	63	99

Table 4: Resolution on the ψ angle as a function of an arbitrary and constant calorimeter angular resolution σ_θ.

2.5 Reconstruction of neutralino lifetime

2.5.1 Reconstruction of decay vertex position

Now that the masses are measured, it becomes possible to fully reconstruct the slepton decay chain. At this stage, a photon conversion inside the volume of the inner detector is no longer needed because the photon direction along ϕ may be inferred indirectly. Therefore the detection volume is notably increased, as the decay of the neutralino is now only required to take place inside the volume delimited by the electromagnetic calorimeter, i.e.

$$r < 156 \text{ cm} \tag{21}$$

$$|z| < 300 \text{ cm} \tag{22}$$

where r is the radial distance to the beam axis.

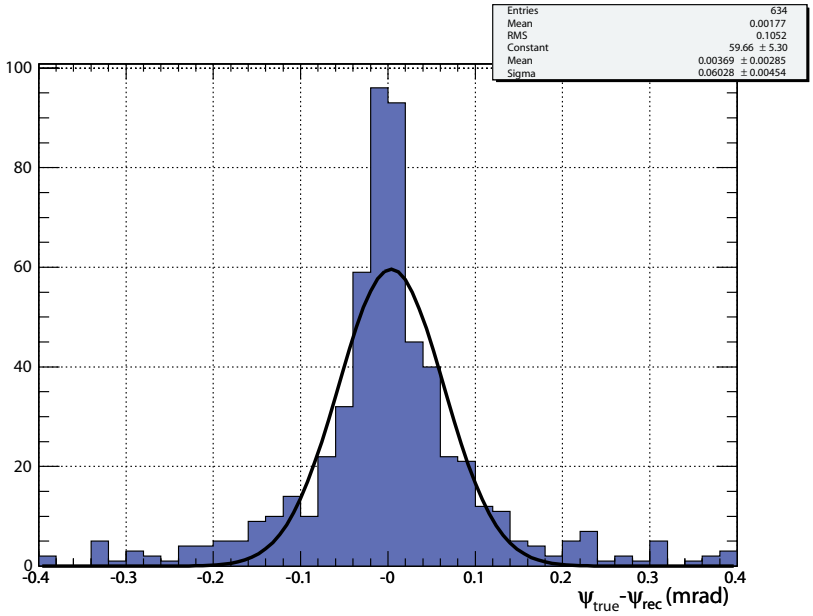

Figure 16: Distribution of the difference between the reconstructed and the true ψ angle, for non-pointing photons selected by the cuts from equation 19.

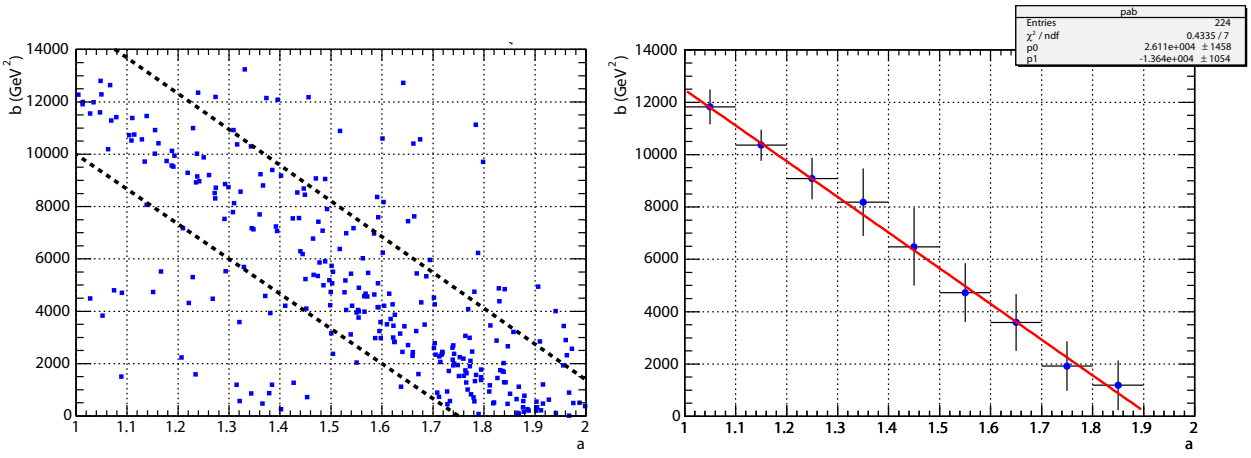

Figure 17: Left plot: distribution of (a, b) parameters for each lepton-photon pair (blue dots). The dashed lines represent the selection area. Right plot: averaged distribution of dots inside the selection area. The red line is the result of a linear fit on the distribution. Only events with a paired lepton $p_T > 20$ GeV enter this plot.

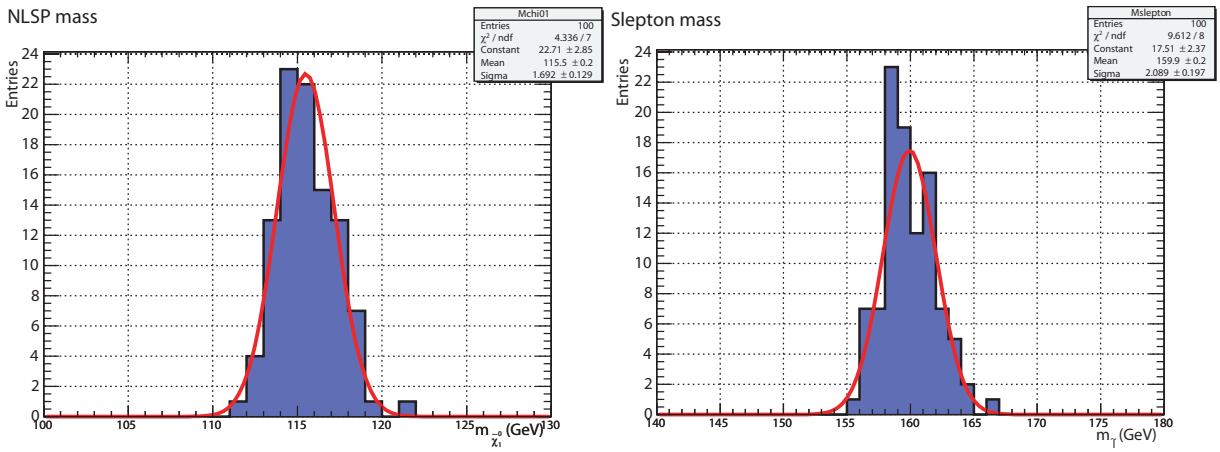

Figure 18: Reconstructed mass of the lightest neutralino (left) and the slepton (right) when simulation is reproduced one hundred times. The true input masses are respectively 117.1 GeV and 161.4 GeV.

If the electromagnetic calorimeter does not allow to measure the photon ϕ direction, this one can be indirectly determined by considering the rest of the decay cascade. Indeed, for each event the following relations have to be simultaneously satisfied:

$$\begin{aligned} t_\gamma &= \frac{OM}{\beta_{\widetilde{\chi}_1^0} c} + \frac{AM}{c} \\ \widetilde{p}_{\widetilde{\ell}}^{\,2} &= \left(\widetilde{p}_{\widetilde{\chi}_1^0} + \widetilde{p}_\ell\right)^2 \\ \widetilde{p}_{\widetilde{\chi}_1^0}^{\,2} &= \left(\widetilde{p}_{\widetilde{G}} + \widetilde{p}_\gamma\right)^2 \end{aligned} \tag{23}$$

where the OA and AM distances refer to figure 11, and where t_γ is the time difference between the interaction and the photon arrival in the calorimeter.

The photon position $\vec{x}_\gamma \equiv \overrightarrow{OA}$ inside the calorimeter, its energy E_γ, its η direction θ and its delay $\Delta t_\gamma \equiv t_\gamma - L/c$ can all be measured for each event. The energy E_ℓ and the momentum $\overrightarrow{p}_\ell$ of the associated lepton are also measured.

The photon impact point $\vec{x}_\gamma$ and polar angle θ_γ define a plane on which is located the neutralino decay vertex $\vec{x}_D$ (figure 19). The decay vertex position must also meet the conditions from 23. These equations can be re-expressed as following:

$$\begin{aligned} E_{\widetilde{\chi}_1^0} E_\ell - \overrightarrow{p}_{\widetilde{\chi}_1^0} \overrightarrow{p}_\ell &= \frac{1}{2}\left[m_{\widetilde{\ell}}^2 - m_{\widetilde{\chi}_1^0}^2 - m_\ell^2\right] \equiv \mathcal{A} \\ E_{\widetilde{\chi}_1^0} E_\gamma - \overrightarrow{p}_{\widetilde{\chi}_1^0} \overrightarrow{p}_\gamma &= \frac{m_{\widetilde{\chi}_1^0}^2}{2} \equiv \mathcal{B} \end{aligned} \tag{24}$$

where the gravitino mass $m_{\widetilde{G}}$ has been neglected. An estimator ξ is then defined as:

$$\xi \equiv \frac{\left|E_{\widetilde{\chi}_1^0} E_\ell - \overrightarrow{p}_{\widetilde{\chi}_1^0} \overrightarrow{p}_\ell - \mathcal{A}\right|}{\mathcal{A}} + \frac{\left|E_{\widetilde{\chi}_1^0} E_\gamma - \overrightarrow{p}_{\widetilde{\chi}_1^0} \overrightarrow{p}_\gamma - \mathcal{B}\right|}{\mathcal{B}} \tag{25}$$

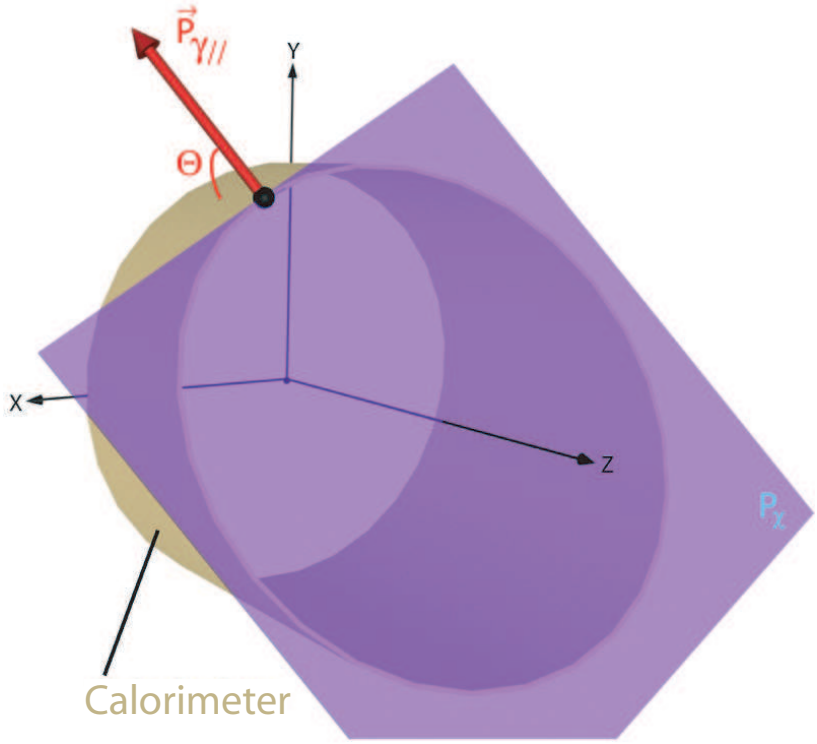

Figure 19: Graphical view of the $\mathcal{P}_\chi$ plane (violet) defined by the incident photon impact point and polar angle θ.

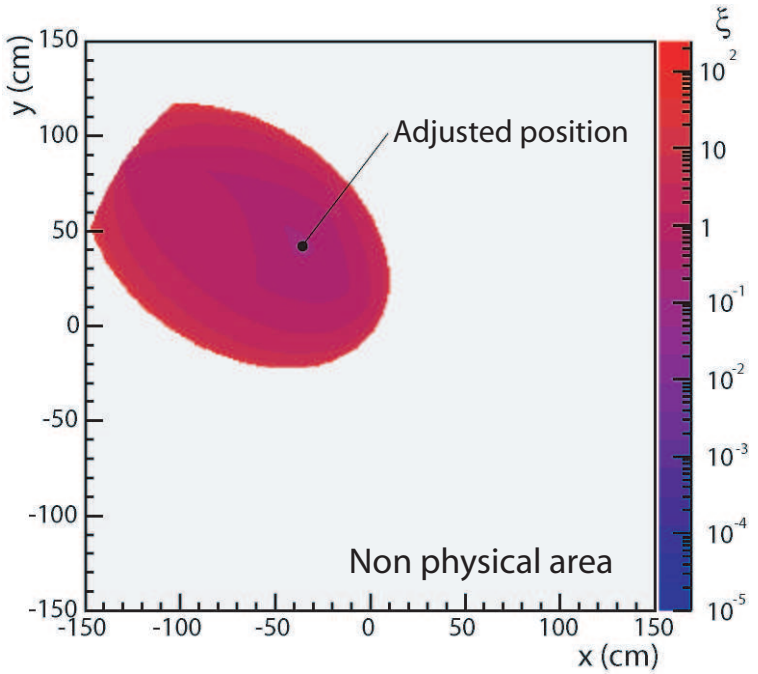

Figure 20: Graphical view of values taken by the ξ estimator for one event. The view is a projection of the $\mathcal{P}_\chi$ plane in the transversal plane XY of the ATLAS detector.

The decay vertex position is obtained by minimizing the values taken by ξ on the $\mathcal{P}_\chi$ plane. For each M point the decay time is calculated, allowing to determine $\beta_{\widetilde{\chi}_1^0}$ and to get the $E_{\widetilde{\chi}_1^0}$ and $\overrightarrow{p}_{\widetilde{\chi}_1^0}$ quantities.

Figure 20 shows the distribution of values taken by ξ for a particular event. Equations 23 leads to two possible solutions. The non-physical solutions and the ones giving a decay vertex outside the calorimeter volume are rejected. When it is possible, only the closest solution to the detector center is kept. A cut on ξ is applied to reject events of which the fit does not converge. A more detailed study is required here to correlate the choice of the good vertex with kinematical or topological variables in order to reach a better efficiency in the vertex selection.

2.6 Analysis

In this part, the same pre-selection cuts as previously are applied (equation 17) and non-pointing photons are selected with the following constraints:

$$\begin{aligned} E_\gamma &> 30 \text{ GeV} \\ \theta_p &> 0.2 \text{ rad} \\ \Delta t_\gamma &> 1 \text{ ns} \end{aligned} \tag{26}$$

where θ_p is defined here as the difference of the polar angles θ_γ and $\theta_{\vec{x}_\gamma}$. This cut is different from the one in equation 19 because in this part the photons ϕ direction is not known. The selection on the θ angle is also less restrictive than the one on the α angle.

The analysis is based on the same set of 10^5 GMSB events used in the previous section, but here the neutralino characteristic decay length $c\tau$ is changed between 10 cm and 2000 cm. An isolated lepton is associated with each non-pointing photon that passes the selection cuts. This lepton must have a 20 GeV minimum transverse momentum. If several leptons are available, only the one that minimizes the $m_{\ell\gamma}$ invariant mass is chosen. For each lepton-photon pair, the neutralino decay vertex is reconstructed using the method described in section 2.5.1. Finally, the neutralino $\beta_{\widetilde{\chi}_1^0}$ function and its lifetime t_D in the laboratory frame are extracted.

The correlation between the true and the reconstructed neutralino lifetime is shown on figure 21 for a characteristic decay length of $c\tau = 100$ cm. The standard deviation of this distribution remains constant at a value of $\sigma \sim 2$ ns over the whole considered $c\tau$ range. The tails of the distributions come from bad lepton-photon pairing or poorly reconstructed decay vertices.

The lifetime t_D corrected for the γ_χ neutralino function for different $c\tau$ values is shown on figure 22. The reconstructed $c\tau$ is determined by fitting an exponential function to the previous distribution. However this requires to have a significant amount of events. In this case, a data set of at least 10^6 events is necessary, corresponding to an integrated luminosity of 100 fb^{-1}.

This study was done for $c\tau$ values varying from 10 cm to 180 cm. In order to study the sensitivity the experiment is reproduced 10 times successively in an independent way for each $c\tau$ value. Results are summarized on figure 23. A systematic bias could be observed as the

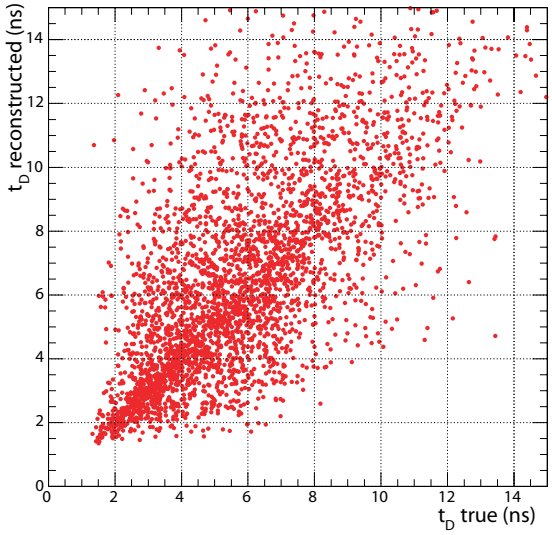

Figure 21: Correlation between the true and the reconstructed neutralino lifetime t_D in the laboratory frame, for $c\tau = 100$ cm.

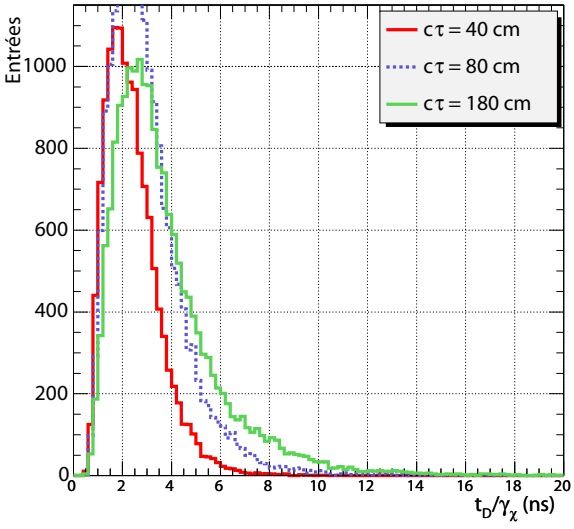

Figure 22: t_D/γ_χ distribution for different $c\tau$ values for an integrated luminosity of 100 fb^{-1}.

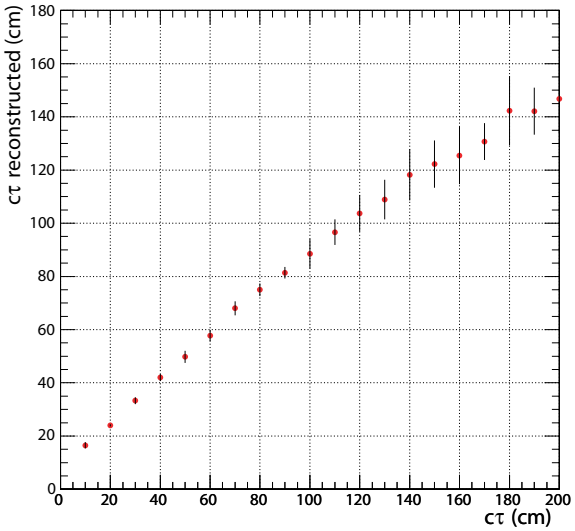

Figure 23: Reconstructed decay length $c\tau$. The experiment is reproduced 10 times for each input $c\tau$ value. Points are the mean values and error bars are the root mean square.

input $c\tau$ value increases. This comes from the fact that neutralino with a higher t_D/γ_χ are more likely to escape the detector without being detected, which bias the t_D/γ_χ distribution. The error bars represent the $c\tau$ root mean square over the 10 reproduced experiments. The sensitivity $\Delta c\tau/c\tau$ is shown on figure 24. For $c\tau < 40$ cm, the sensitivity is below 3% but quickly increases to 8% for $c\tau = 180$ cm.

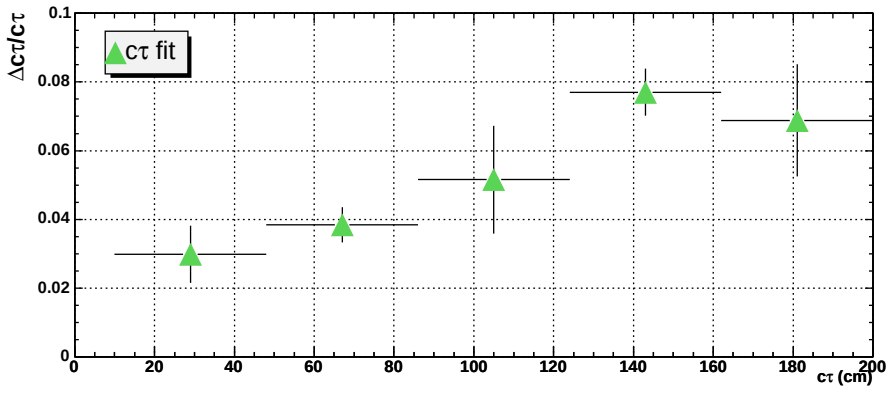

Figure 24: Sensitivity on the measure of the $\widetilde{\chi}_1^0$ lifetime $c\tau$.

2.7 Sensitivity on $\sqrt{F_0}$

The neutralino lifetime is linked to the fundamental supersymmetric breaking scale $\sqrt{F_0}$ by the equation 9, hence the determination of the $c\tau$ parameter allows to constraint $\sqrt{F_0}$. The

previous section has shown that the resolution on $c\tau$, in the range from 10 to 200 cm, is typically of the order of 5%. For $c\tau$ = 100 cm, the study from section 2.4 shows that a resolution of 2% on the neutralino mass could be expected. In that case, the sensitivity $\Delta\sqrt{F_0}/F_0$ on the fundamental supersymmetric breaking scale is 4% for a value of 1200 TeV and the sensitivity on the gravitino mass is 8% for a mass of 0.3 keV.

2.8 Trigger and background

2.8.1 Triggering on events with 2 non-pointing photons

The topology of the considered events is the following:

- A high energy lepton pair
- A isolated lepton pair
- Jets
- Missing energy

These events would pass the level-1 trigger selection thanks to high transverse energy jets (4j110) and to the two photons ($2\gamma 20i$). The reconstructed energy by the standard algorithms that are used by the level-2 trigger are sufficient to ensure a good trigger efficiency for such events. Biases on the reconstructed energy do not exceed 6% for non-pointing photons with p_T = 60 GeV, generated from an effective vertex at Z_{vertex} = 150 cm.

A more detailed study of the triggering efficiency would require to check the effects introduced by the energy and time reconstruction algorithms performed in the read-out drivers for each cell. Indeed, the particle time arrival is dominated by the time measurement of the most energetic cell in the cluster. This time is reconstructed using an optimal filtering technique from the five samples of the physics signal with respect to a reference time. Reconstruction performance will need to be studied for particle with such a time lag (several nanoseconds). It may be interesting to know if it would be possible for the algorithm to transfer the digitization values in the case the energy in greater than 10-20 GeV and the signal shape different from a reference one.

2.8.2 Signal background

Events studied here, predicted from GMSB models with long lived neutralinos, have two high transverse momentum photons. This topology allows to reduce considerably the background. The main background sources for this channel come from Standard Model processes [15]:

- Processes with bad photon identification and missing energy (figure 25).
- Processes with missing energy due to a bad reconstruction of the energy balance.

Selection cuts described in this section allow to reduce these contributions. Studies made by $D\emptyset$ and CDF show that the background level may be constraint not to perturb the detection of GMSB events and the reconstruction of the model parameters. Studies made by $D\emptyset$ and CDF were looking for pointing photons; here they are mainly non-pointing and time lagged; these two characteristics will allow to suppress more effectively the background.

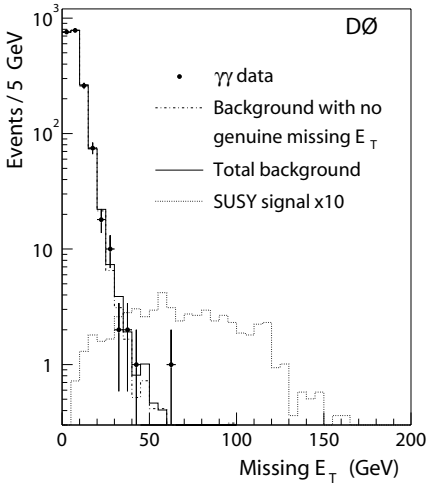

Figure 25: Missing energy distribution for di-photons events and for the background of the $D0$ experiment [15]. The expected GMSB signal is also represented for $\Lambda = 80$ TeV and $\sqrt{s} = 1.8$ TeV.

2.9 Conclusion

In this section a realistic electromagnetic calorimeter angular resolution has been implemented in a fast simulation of the ATLAS detector. With such performance, it has been shown that it is possible to reconstruct the neutralino and slepton masses with a 2% precision. It is also possible to get a sensitivity close to 5% on the neutralino lifetime, leading to a determination of the fundamental supersymmetric breaking scale within 4% for $c\tau$ between 10 to 200 cm.

The results in this section do not take into account systematics errors from measurements and only the statistical uncertainty is taken into account. The detector systematics will require a careful study from a detailed detector simulation.

Probable sources of systematic errors are:

- Effects of pile-up and underlying events on the direction reconstruction
- Quality of the electromagnetic shower description.

This study shows that it would possible to extract a GMSB supersymmetric signal in case the NLSP is the lightest neutralino and for a characteristic lifetime from 10 to 200 cm.

Acknowledgements

I would like to thank Giacomo Polesello and Isabelle Wingerter-Seez for their valuable advices all along this study. Giacomo helped me to set up the various Monte Carlo generators and guided me, answering my questions. I am grateful to Isabelle for her help understanding the electromagnetic calorimeter performance from the simulation.

List of Figures

References

[1] ATLAS detector and physics performance. Technical design report. Vol. 1. CERN-LHCC-99-14.

[2] A. Artamonov, A. Dell'Acqua, D. Froidevaux, M. Nessi, P. Nevski, and G. Poulard. ATLAS-SOFT/95-14c.

[3] For information concerning ATLAS reconstruction tools, see the *offline software* webpage. http://atlas.web.cern.ch/Atlas/GROUPS/SOFTWARE/OO/Applications/.

[4] J. Colas et al. Position resolution and particle identification with the atlas em calorimeter. *Nucl. Instrum. Meth.*, A550:96–115, 2005.

[5] G. F. Giudice and R. Rattazzi. Theories with gauge-mediated supersymmetry breaking. *Phys. Rept.*, 322:419–499, 1999.

[6] S. Ambrosanio, Gordon L. Kane, Graham D. Kribs, Stephen P. Martin, and S. Mrenna. Search for supersymmetry with a light gravitino at the fermilab tevatron and cern lep colliders. *Phys. Rev.*, D54:5395–5411, 1996.

[7] Kiyotomo Kawagoe, Tomio Kobayashi, Mihoko M. Nojiri, and Atsuhiko Ochi. Study of the gauge mediation signal with non-pointing photons at the cern lhc. *Phys. Rev.*, D69:035003, 2004.

[8] ATLAS detector and physics performance. Technical design report. Vol. 2. CERN-LHCC-99-15.

[9] G. Corcella et al. HERWIG 6: An event generator for hadron emission reactions with interfering gluons (including supersymmetric processes). *JHEP*, 01:010, 2001.

[10] E. Richter-Was, D. Froidevaux, and L. Poggioli. ATLFAST 2.0 a fast simulation package for ATLAS. ATL-PHYS-98-131.

[11] Frank E. Paige, Serban D. Protopescu, Howard Baer, and Xerxes Tata. ISAJET 7.69: A Monte Carlo event generator for p p, anti-p p, and e+ e- reactions. 2003.

[12] I. Nikolic-Audit. Time resolution of the ATLAS barrel liquid argon electromagnetic calorimeter. ATL-LARG-2004-002.

[13] ATLAS inner detector: Technical design report. Vol. 1. CERN-LHCC-97-16.

[14] I. Hinchliffe and F. E. Paige. Measurements in gauge mediated SUSY breaking models at LHC. *Phys. Rev.*, D60:095002, 1999.

[15] V. M. Abazov et al. Search for supersymmetry with gauge-mediated breaking in diphoton events at D0. 2004. hep-ex/0408146.